Influence of Al-substitution on structural, electrical and magnetic properties of Mn–Zn ferrites nanopowders prepared via the sol–gel auto-combustion method

M.A. Gabal [a,*], A.M. Abdel-Daiem [b,c], Y.M. Al Angari [a], I.M. Ismail [a,d]

[a] Chemistry Department, Faculty of Science, King Abdulaziz University, Jeddah, Saudi Arabia
[b] Physics Department, Faculty of Science, King Abdulaziz University, Jeddah, Saudi Arabia
[c] Physics Department, Faculty of Science, Zagazig University, Zagazig, Egypt
[d] Center of Excellence in Environmental Studies, King Abdulaziz University, PO Box 80216, Jeddah, 21589, Saudi Arabia

ARTICLE INFO

ABSTRACT

A series of nano-sized Al-substituted manganese zinc ferrites, $Mn_{0.8}Zn_{0.2}Fe_{2-x}Al_xO_4$ ($x = 0.0-1.0$), with a cubic spinel crystal structure were prepared through the citrate sol–gel auto-combustion method. Thermogravimetric measurements revealed that the optimum calcination temperature for complete formation of ferrites is 300 °C. At higher calcination temperatures X-ray diffraction indicated the presence of Fe_2O_3 and Mn_2O_3 secondary phases, attributed to the ferrites decomposition. The average crystallite size, calculated using the Debye–Scherrer equation, lies in the range 5–38 nm. The gradual decrease in lattice parameter with increasing Al-content can be attributed to the smaller ionic radii of the Al^{3+} ion. The TEM image showed large agglomerates of strongly connected cubic aggregates. FT-IR spectra exhibited two prominent absorption bands, v_1 and v_2, characteristic for the spinel structure. VSM measurements indicated a gradual decrease in the saturation magnetization with increasing Al-content, until it vanished at $x = 0.8$, followed by a slight increase. The reduction in coercivity with increasing Al-content can be ascribed to the effect of magneto-crystalline anisotropy. Based on XRD, FT-IR and VSM studies, an appropriate cation distribution for the present investigated system was suggested. The temperature dependence of the AC-conductivity as a function of the applied frequency showed semiconducting behavior with a transformation in the conduction mechanism from the ferrimagnetic to the paramagnetic state for ferrites with $x \leqslant 0.4$.

1. Introduction

Soft ferrites with a spinel structure find potential applications in electrical components, memory devices, magnetostrictive and microwave devices over a wide range of frequencies because of their high resistivity and low losses [1]. The field of ferrites is well cultivated, owing to their various potential applications and the interesting physics involved in them.

Among these ferrites, manganese–zinc ferrites are preferred over other ferrites because of their high initial permeability, low losses, high resistivity, high saturation magnetization and relatively high Curie temperature [2]. They have attracted considerable attention in high frequency applications, such as magnetic recording materials, multi-layer chip inductors, electromagnetic interference shielding and gas sensors [3–6].

The structural, magnetic and electrical properties of ferrites are found to be sensitive to their composition and microstructure, which in turn are dependent on the processing conditions and different synthesis routes [1]. Recently fine particles of spinel ferrites synthesized by wet-chemical methods were shown to have markedly different magnetic properties from those prepared by the ceramic method [7].

Several chemical processing techniques are available for the synthesis of ferrites [8–13]. The selection of an appropriate synthetic procedure often depends on the desired properties and the final applications. Among these methods, the citrate sol-gel auto-combustion method has several advantages over others for the preparation of nanosized compounds [14].

Additive materials can occupy different positions on the tetrahedral or octahedral sites and alter the magnetic, electrical or microstructure properties of ferrites. By this way, the different properties can be tailored to suit a particular application [15].

Numerous studies on the effect of the additives to Mn–Zn ferrites have been carried out in the literature. Hankare et al. [1] studied the effect of Cr^{3+} ion substitution in nanocrystalline

* Corresponding author. Address: Chemistry Department, Faculty of Science, Benha University, Benha, Egypt. Tel.: +20 966557071572.
E-mail address: mgabalabdonada@yahoo.com (M.A. Gabal).

$ZnMn_{1-x}Cr_xFeO_4$ ($1.0 \geqslant x \geqslant 0$) prepared by the sol-gel route. XRD, TEM and IR techniques have been used to determine the role of the substitution on the structural properties. Venkataraju et al. [16] synthesize nanoparticles of $Mn_{0.5}Zn_{0.5-x}Cd_xFe_2O_4$ (x = 0.0, 0.1, 0.2 and 0.3) by the co-precipitation method. XRD indicated a deviation in the cation distribution. The dielectric constant, dielectric loss and the magnetization are observed to decrease with the Cd content. Song et al. [17] prepared magnesium-substituted Mn–Zn ferrites with the composition $Mn_{0.4}Zn_{0.6}Mg_xFe_{2-x}O4$ (x = 0.00 and 0.05) by the citrate–EDTA complexing method. Studying the crystal structure, surface morphology and electromagnetic properties of the substituted ferrites indicated that the Mg-substitution enhanced the microwave absorbing performance. Brusentsova and Kuznetsov [18] synthesized nanoparticles of $Mn_{1-x}Zn_x[Fe_{2-y}L_y]O_4$ ferrites (where L: Gd^{3+}, La^{3+}, Ce^{3+}, Eu^{3+}, Dy^{3+}, Er^{3+}, Yb^{3+}) by the co-precipitation method. The absence of a hysteresis loop in the M–H curve indicates superparamagnetic properties. Zhang et al. [19] prepared Mn–Zn ferrite nanoparticles with various amounts of cobalt doping by the co-precipitation method. The effects of cobalt ions on the crystallization behavior, lattice parameters and magnetic properties of Mn–Zn ferrites have been investigated. Ateia et al. [20] measured the dielectric constant, AC conductivity and Seebeck coefficient for $Mn_{0.5}Zn_{0.5}R_yFe_{2-y}O_4$ ferrites (R = Dy, Gd, Sm, Ce and La) prepared by the standard ceramic technique. It was found that the addition of rare earth ions to the system acts as a sintering catalyst, which helps in the development of a solid solution at lower temperatures. Brusentsova et al. [21] synthesized Gd-substituted Mn–Zn ferrite nanoparticles of different compositions by the co-precipitation method. The magnetic properties dependence on the composition and cationic distribution were investigated. Arora et al. [22] studied the effect of Gd^{3+} ion substitution in $Mn_{0.5}Zn_{0.5}Gd_xFe_{2-x}O_4$ ferrites nanoparticles (x = 0.1, 0.2, 0.3, 0.4) on the structural, morphological and magnetic properties. The Gd^{3+} ions were found to present in the interstitial sites of the ferrite lattice, which causes the variation in these nanoparticles. Ahmed et al. [23] studied the effect of rare-earth ions on the structural, magnetic and electrical properties of $Mn_{0.5}Zn_{0.5}R_{0.05}Fe_{1.95}O_4$ ferrites (R = Tb, La, Ce and Th), prepared by the flash combustion technique. The results revealed that the introduction of rare earths enhanced the structure and physical properties. Chandrasekaran et al. [24] prepared Al-substituted Mn–Zn ferrites by the ceramic method. Confirmation of the single-phase and cation distribution were confirmed using XRD. The change in the electrical properties are discussed as a function of the Al concentration. Saafan et al. [25] have tried to find the best realistic theoretical methods to analyze experimental data taken for Al-substituted Mn–Zn spinel ferrites.

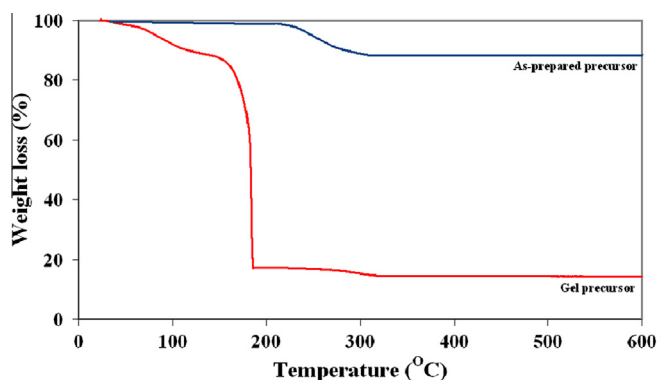To the best of our knowledge, there are no works about the effect of Al-substitution on the different properties of Mn–Zn ferrites, prepared through the sol-gel method, in the literature. In view of this, we studied the effect of Al-substitution on the composition, microstructure, sizes and electromagnetic properties of nano-crystalline $Mn_{0.8}Zn_{0.2}Fe_{2-x}Al_xO_4$ (x = 0.0–1.0), prepared through the citrate sol-gel auto-combustion method. The compositions were characterized by DTA-TG, FT-IR and XRD. The particle size and morphology were investigated by transmission electron microscopy (TEM). The corresponding changes in the magnetic properties were studied using the vibrating sample magnetometer technique (VSM). The AC electrical conductivity as a function of frequency and temperature was measured to predict the possible conduction mechanisms and to calculate the conduction activation energies.

2. Experimental procedures

2.1. Material preparation

All reagents used were of analytical grade. The $Mn_{0.8}Zn_{0.2}Fe_{2-x}Al_xO_4$ ferrites (x = 0.0–1.0) were synthesized by the sol–gel citrate auto-combustion method. The reagents used in this work are ferric nitrate ($Fe(NO_3)_3 \cdot 9H_2O$), zinc nitrate ($Zn(NO_3)_2 \cdot 6H_2O$), manganese nitrate ($Mn(NO_3)_2 \cdot 4H_2O$), aluminum nitrate ($Al(NO_3)_3 \cdot 9H_2O$), citric acid ($C_6H_8O_7$) and ammonium hydroxide.

Firstly, stoichiometric amounts of the metal nitrates and citric acid were weighed (1:1 mole ratio) and dissolved in distilled water at 60 °C for 30 min. Then, ammonium hydroxide was added dropwise under constant stirring up to pH 7. The solution was further heated at 80 °C until it transformed into a gel. On ignition, violent combustion occurred, which spontaneously propagated until all the gel was completely burnt out to form a loose powder, named the as-prepared citrate precursor samples. The powders were then calcined at 300 °C for 1 h or at 500 or 700 °C for 2 h.

2.2. Characterization

Thermal decomposition behavior of the precursor (in the form of a gel) was characterized using thermogravimetry measurements (TG). The measurements were taken in air using a Perkin Elmer thermal analyzer up to 600 °C, at a heating rate of 5 K min⁻¹. All the synthesized samples were characterized by XRD using a Bruker axs diffractometer, with Cu Kα radiation and a secondary monochromator in a 2θ range from 10° to 70°. The average crystallite size of the samples was estimated using Scherer's equation [26]. TEM was performed using a JEOL 2010 TEM (100 kV). The sample was dispersed in ethanol using an ultrasonicator and then loaded over coated copper grids. FT-IR spectra were recorded using a Perkin Elmer FT-IR spectrometer in KBr medium in the range 700–200 cm⁻¹. The room temperature magnetization measurements, up to a maximum field of 5 kOe, were carried out using a vibrational sample magnetometer (VSM-9600M). The temperature dependence of the dielectric constant, dissipation factor and ac conductivity measurements were studied, using the two probe method by a Hioki LCR bridge model 3531 in the frequency range 50 Hz–5 MHz. The ferrite samples were compressed to pellets of 1 cm diameter and about 1 mm thickness. The pellet surfaces were polished and coated with silver paint. The temperature of the sample was measured using a K-type thermocouple.
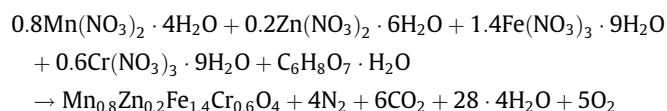
3. Results and discussion

3.1. Thermal decomposition behavior of the precursors

The thermal decomposition behavior of the gel as well as the as-prepared precursor with x = 0.6 are illustrated in Fig.1. The figure shows that instead of the three well-defined TG steps,

Fig. 1. TG curves in air of precursors with an Al-content of 0.6. Heating rate = 5 °C min⁻¹.

characterizing the gel decomposition, only one TG step accompanies the decomposition of the as-prepared precursor. For the gel precursor, the first step up to 150 °C can be attributed to the gel dehydration process. The second step is the main decomposition step and exhibits a steep weight loss, amounting to 73% at 188 °C, which is attributed to the violent decomposition of the NH_4NO_3 contents of the gel. The precursor is observed to be thermally stable up to 275 °C, then its citrate contents starts to decompose in the third step, exhibiting a weight loss of 3.5%. Beyond 310 °C, no further weight loss can be detected.

The thermo-gram of the as-prepared precursor showed a weight loss change up to 320 °C. Consistent with the above discussion, this weight loss can be assigned to the decomposition of the residual citrate content. Thus we can conclude that the heat evaluated during the auto-combustion reaction will be not enough for ferrite formation and further calcination at 300 °C is required.

The typical nitrate–citrate auto-combustion reaction for the entire precursor can be presented as [27]:

$$0.8Mn(NO_3)_2 \cdot 4H_2O + 0.2Zn(NO_3)_2 \cdot 6H_2O + 1.4Fe(NO_3)_3 \cdot 9H_2O$$
$$+ 0.6Cr(NO_3)_3 \cdot 9H_2O + C_6H_8O_7 \cdot H_2O$$
$$\rightarrow Mn_{0.8}Zn_{0.2}Fe_{1.4}Cr_{0.6}O_4 + 4N_2 + 6CO_2 + 28 \cdot 4H_2O + 5O_2$$

3.2. X-ray diffraction

The effect of the calcination temperature on the structure and phase formation of the investigated precursors was monitored using the XRD technique. The XRD patterns of the as-prepared precursors (Fig. 2) showed the absence of any diffraction lines attributed to the presence of metal oxides and confirm the formation of a single-phase spinel structure. The diffraction peaks can be indexed to $(220), (311), (222), (400), (422), (511)$ and (440) planes of the cubic unit cell.

The obvious broadening of all the diffraction peaks indicates the nano-sized particle nature of the obtained ferrites. Crystallization of the samples became more difficult and some sort of amorphous-like phases were obtained for the samples with a higher Al-content ($x > 0.6$). This indicates that excessive addition of Al inhibits the crystal growth.

In agreement with the TG results, the crystallinity of the samples increased by increasing the calcination temperature to 300 °C (Fig. 3). This can be due to the disappearance of the residual citrate content. The average crystallite size (L), calculated using the Debye–Scherrer equation [26], lies in the range 5–38 nm and exhibited a gradual decrease with increasing Al-content.
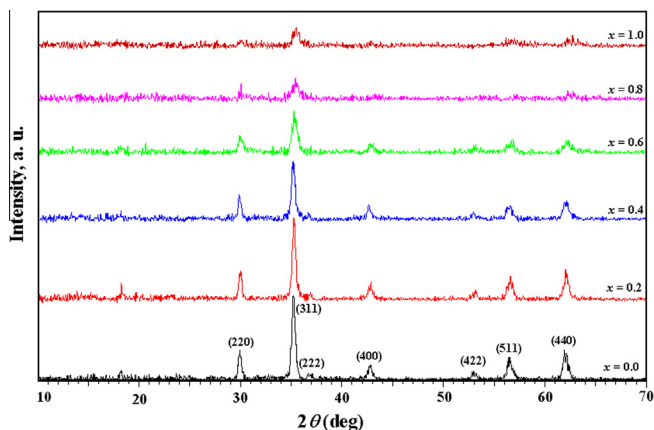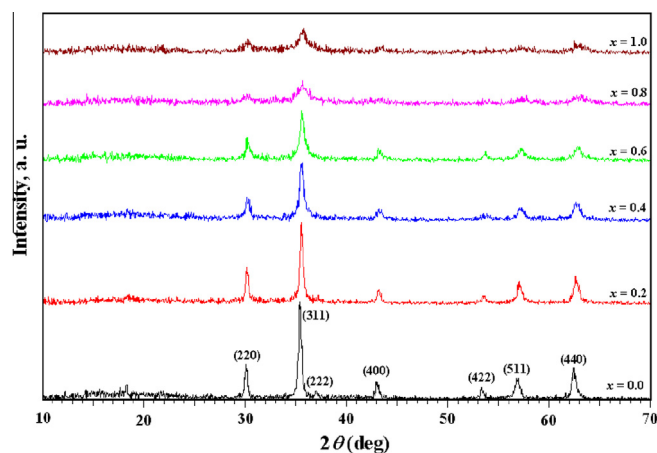

Fig. 3. XRD patterns of the precursors calcined at 300 °C.

Fig. 3 also shows a gradual shift in the peaks positions towards higher 2θ angles by increasing the Al-content. In agreement with this observation, the lattice parameter calculated from this displacement decreases with increasing Al-content. This can be attributed to the smaller ionic radius of the Al^{3+} ion (oct: 0.535 Å), which has a strong octahedral site preference [28], compared to the ionic radii of the substituted Fe^{3+} ion (0.645 Å). The partial replacement of Fe^{3+} by Al^{3+} will then be expected to cause shrinkage of the unit cell. Moreover, the higher binding energy and bond strength of Al–O compared to Fe–O [29] cannot be ignored. The obtained values of the lattice parameters exhibited a linear content dependence, thus obeying the Vegard's law [30], as can be shown in Fig. 6. The above variation in both the crystallite size and lattice parameters is in full agreement with the experimental results of most of the previous works [28,29,31].

The X-ray density (D_x) depends on both the lattice constants and the molecular weight of the investigated sample. It shows gradual decreases with increasing Al-content (Fig. 4). This can be due to the decrease in the lattice parameters by the substitution of the heavier atomic weight iron with the lower atomic weight aluminum.

$ZnFe_2O_4$ is a well-known normal spinel [32], however its nano-sized properties may lead to the formation of inverse-spinel zinc ferrites [33–35]. Mn^{2+} ions have a strong preference for the octahedral sites, but using X-ray absorption fine structure and Mössbauer measurements [36,37] they exhibit a disorder between both sites. Fe^{3+} ions can exist at both sites, though they prefer the B site [38].

Thus, regarding the obtained experimental lattice parameter (a_{exp}) and based on the above expectations, an appropriate cation
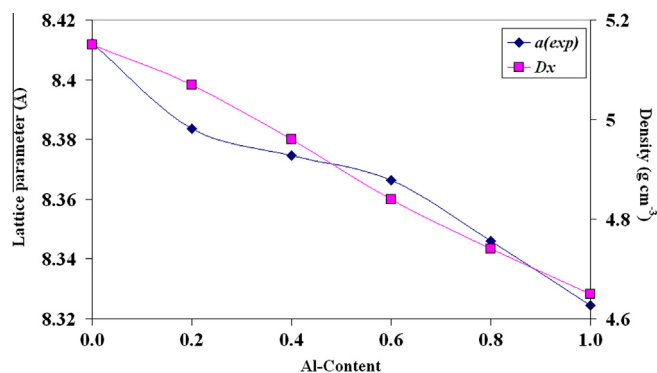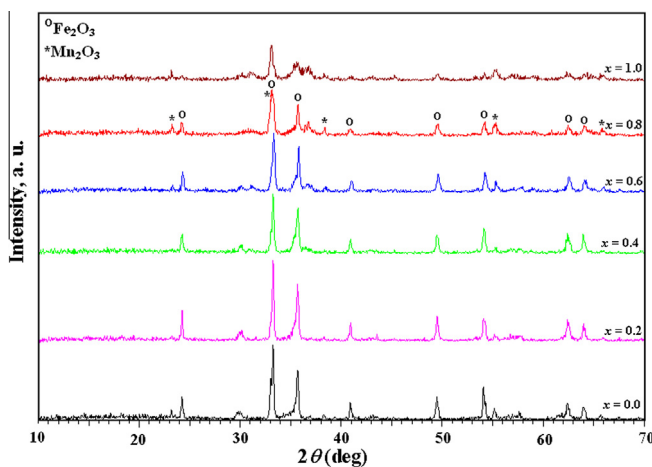

Fig. 2. XRD patterns of the as-prepared precursors.

Fig. 4. Variation of the lattice parameters and X-ray density with x in the $Mn_{0.8}Zn_{0.2}Fe_{2-x}Al_xO_4$ system.

Table 1
Structural, magnetic and electrical data of the $Mn_{0.8}Zn_{0.2}Fe_{2-x}Al_xO_4$ system.

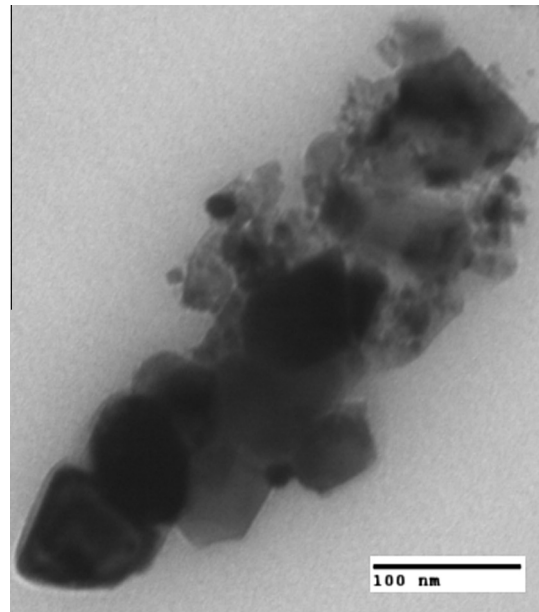| Cation distribution	a (Å)		r (Å)		L (nm)	D_x (g cm^{-3})	γ	L_A (Å)	L_B (Å)	v_1 (cm^{-1})	v_2 (cm^{-1})	M_S	M_r	H_C	η_B	η_B (x)	E_f (eV)	(E_p) (eV)	$\sigma \times 10^{-6}$
	a_{exp}	a_{th}	r_A	r_B															
$(Mn_{0.3}Zn_{0.2}Fe_{0.5})[Mn_{0.5}Fe_{1.5}]O_4$	8.4123	8.4074	0.563	0.651	38	5.15	0.5	3.643	2.974	570	428	45.2	15.9	200	1.87	6	0.78	0.90	4.33
$(Mn_{0.3}Zn_{0.2}Fe_{0.5})[Mn_{0.5}Fe_{1.3}Al_{0.2}]O_4$	8.3836	8.3780	0.563	0.640	25	5.07	0.5	3.630	2.968	572	450	37.9	11.7	160	1.53	5	0.81	0.99	2.51
$(Mn_{0.3}Zn_{0.2}Fe_{0.5})[Mn_{0.5}Fe_{1.1}Al_{0.4}]O_4$	8.3635	8.3494	0.563	0.629	17	4.98	0.5	3.621	2.960	577	455	30.1	6.5	62	1.18	4	0.91	1.02	2.22
$(Mn_{0.3}Zn_{0.2}Fe_{0.5})[Mn_{0.5}Fe_{0.9}Al_{0.6}]O_4$	8.3544	8.3201	0.563	0.618	12	4.86	0.5	3.617	2.957	581	–	26.5	5.4	–	1.01	3	–	1.06	2.11
$(Mn_{0.3}Fe_{0.7})[Mn_{0.5}Fe_{0.5}Zn_{0.2}Al_{0.8}]O_4$	8.3329	8.2823	0.541	0.617	6	4.77	0.7	3.608	2.950	581	–	6.3	0.6	47	0.23	0	–	1.16	1.61
$(Mn_{0.3}Fe_{0.7})[Mn_{0.5}Fe_{0.3}Zn_{0.2}Al]O_4$	8.3105	8.2529	0.541	0.606	5	4.67	0.7	3.598	2.942	582	–	7.0	0.8	31	0.26	1	–	1.28	0.91
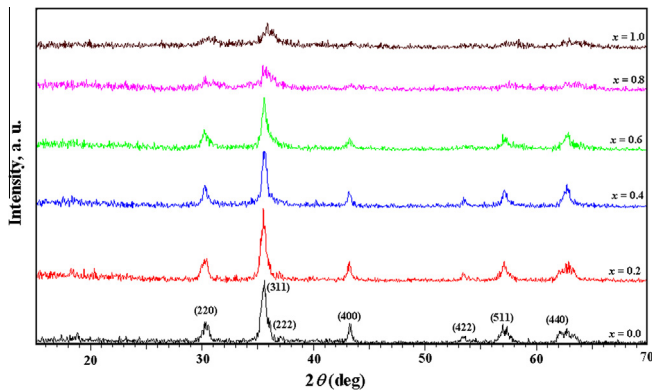
Fig. 5. XRD patterns of the precursors calcined at 500 °C.

Fig. 6. XRD patterns of the precursors calcined at 700 °C.

Fig. 7. TEM image of the sample with x = 0.6.

X-ray diffraction patterns of the precursors calcined at 500 °C (Fig. 5) showed an obvious splitting of the diffraction lines attributed to the spinel structure, which indicates the starting of the formation of other phases. This is more obvious in the case of precursors calcined at 700 °C (Fig. 6). The appearance of new intense peaks, which can be assigned to Fe_2O_3 (JCPDS No. 79-1741) and Mn_2O_3 (JCPDS No. 73-1826), besides those attributed to the spinel structure, can be attributed to the ferrites decomposition.

3.3. TEM

A typical TEM image of the precursor calcined at 300 °C with x = 0.6 is shown in Fig. 7. The image shows large agglomerates of strongly connected cubic aggregates. This agglomeration can be due to the experience of nano-sized magnetic fine particles with a permanent magnetic moment proportional to their volume. Hence, each particle is permanently magnetized and gets agglomerated [40].

3.4. FT-IR spectral study

Fig. 8 shows the FT-IR spectra of precursors calcined at 300 °C. The spectra show two prominent absorption bands, v_1 and v_2, at about 600 and 400 cm^{-1}, respectively, which confirms the formation of the spinel structure. The higher frequency band and lower frequency band are assigned to the intrinsic vibrations of tetrahedral and octahedral sites respectively [41]. The band positions of
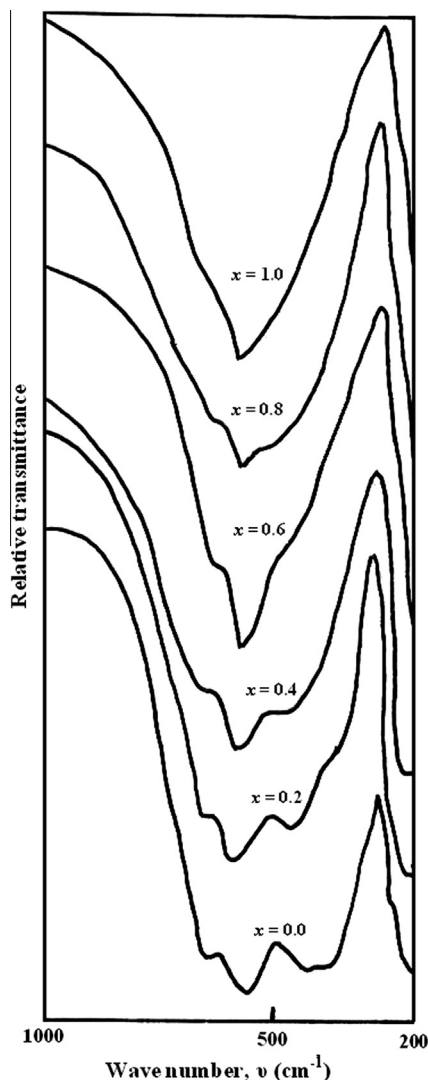
distribution can be suggested. The suggested cation distributions of the investigated ferrites, along with the calculated ionic radii for their tetrahedral and octahedral sites, the inversion factor (γ) and the resultant theoretical lattice parameters (a_{th}) [26] are reported in Table 1. From the results it is clear that the theoretically calculated lattice parameters agree well with those obtained experimentally, with a slight deviation observed for high Al-content samples.

The hopping lengths of the A-sites (L_A) and B-sites (L_B) were calculated using an equation from [39]. The gradual decrease in the length between the magnetic ions (Table 1) with Al-substitution can be explained on the basis of ionic radii. The gradual substitution with the smaller Al^{3+} ions makes the magnetic ions come closer to each other, decreasing the hopping length.

Fig. 8. FT-IR spectra of the $Mn_{0.8}Zn_{0.2}Fe_{2-x}Al_xO_4$ system.

Fig. 9. Hysteresis loops for the $Mn_{0.8}Zn_{0.2}Fe_{2-x}Al_xO_4$ system.

Fig. 10. Variation of the saturation magnetization and coercivity with x in the $Mn_{0.8}Zn_{0.2}Fe_{2-x}Al_xO_4$ system.

the investigated samples are tabulated in Table 1. The intensity of the v_2 band goes on decreasing up to $x = 0.6$ and then vanishes completely. This behavior agrees well with that reported by Kawade et al. [42,43].

The higher frequency band, v_1, shows a very slight shift with increasing Al-content, whereas the lower frequency band, v_2, obviously increased. This behavior agrees well with the reported radii of tetrahedral and octahedral sites (Table 1). In addition, it suggests the preferential occupancy of Al^{3+} ions, with a smaller radius and lower atomic weight, for octahedral sites (which will affect and support the assumption made regarding the cation distribution, Table 1).

3.5. Hysteresis studies

The $M–H$ curves can be helpful in understanding the magnetic response of the synthesized materials and can provide information regarding magnetic parameters, such as saturation magnetization (M_s), coercivity (H_c) and remanent magnetization (M_r). Fig. 9 shows the variation of magnetization as a function of applied magnetic fields for the investigated ferrites, measured at room temperature. The magnetic data obtained are summarized in Table 1 and Fig. 10.
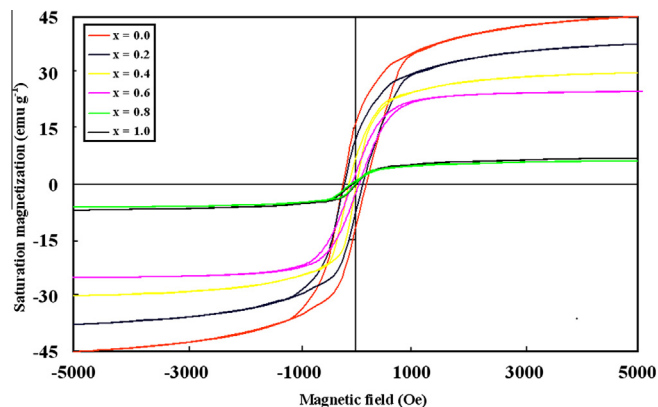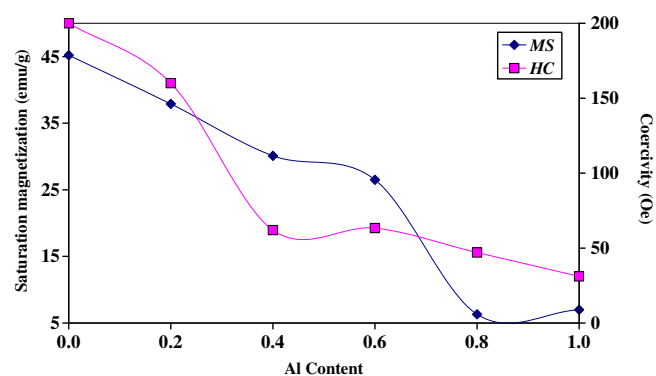
From the table it is clear that the magnetization decreases with increasing Al content. The substitution of Fe^{3+} ions by diamagnetic Al^{3+} ions, which have a stronger preference for occupying the octahedral sites, decreases the magnetic moment and consequently the net magnetization through weakening of A–B interactions and disturbing of the spin ordering. The observed magnetic moment (η_B) per formula unit in Bohr magnetons (μ_B) was calculated using the formula [26]:

$$\eta_B = MW \times M_S/5585$$

where MW is the molecular weight of the sample and M_S is the saturation magnetization in emu/g.

According to Neel's two sub-lattice model of ferrimagnetism [44], the calculated magnetic moment per formula unit can be expressed as:

$$\eta_B(x) = M_B(x) - M_A(x)$$

where M_A and M_B are the sub-lattice magnetic moments of the A and B sites, respectively. This can be achieved using the proposed cation distribution (Table 1) and the ionic magnetic moment of Fe^{3+} (5 μ_B), Mn^{2+} (5 μ_B), Zn^{2+} (0 μ_B) and Al^{3+} (0 μ_B). The observed and calculated magnetic moments of the investigated system are reported in Table 1. From the table it is obvious that both values show a decreasing trend with increasing Al-content.

This subsequent decrease in magnetization and consequently decrease in magnetic moment continues up to $x = 0.6$. By further substitution of Al^{3+} ($x = 0.8$), the net magnetic moments of both octahedral and tetrahedral sites, according to the proposed cation distribution, becomes nearly equal and lead to a zero magnetic moment. With an Al-content of 1.0, the magnetic moment of the
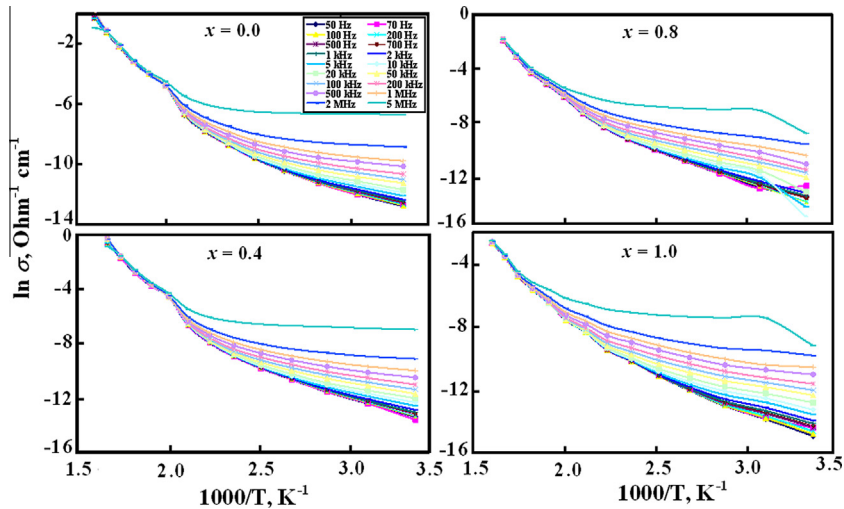
Fig. 11. Relation between ln σ and the reciprocal of absolute temperature at different Al-contents as a function of applied frequency for the $Mn_{0.8}Zn_{0.2}Fe_{2-x}Al_xO_4$ system.

tetrahedral site predominates and the direction of the magnetization is inversed. This results, as appears in Table 1, in increasing the magnetization of the sample with $x = 1.0$ relative to that with $x = 0.8$. The remanent magnetization (M_r) showed a similar behavior to that reported for saturation magnetization.

The reduction in coercivity with increasing Al-content can be ascribed to the effect of magneto-crystalline anisotropy. Al^{3+} ions have zero angular momentum ($l = 0$) [29] and thus do not contribute to the magneto-crystalline anisotropy. When Al replaces iron, the spin–orbit coupling is weakened resulting in a decrease in the magnetic coercivity.

3.6. AC-conductivity measurements

Fig. 11 illustrates typical curves correlating the temperature dependence of the AC-conductivity for the investigated ferrites as a function of applied frequency. From the figure it is clear that the investigated samples have semi-conducting behavior, in which conductivity increases with increasing temperature.

In the low temperature region, the conductivity slightly increases with increasing temperature and is strongly frequency dependent. In this region, the thermal energy is not enough to liberate charge carriers and increasing the frequency enhances their hopping. By increasing the temperature the conductivity becomes frequency independent and a linear relation was obtained. Such conductivity increases can be related to the increase in the drift mobility of thermally activated charge carriers according to hopping conduction mechanism.

The obvious change in the slope of this linear relation can be attributed to the change in the conduction mechanism, arising from the transformation from the ferrimagnetic to paramagnetic state. Similar transitions have also been reported for various ferrite systems [45,46]. At higher Al-content ($x > 0.4$), this transition disappeared, which suggests the paramagnetic properties of these samples at low temperature. The activation energies in the ferri- and paramagnetic regions (E_f and E_p) are calculated from the slopes of ln σ versus $1000/T$ (at 1 kHz) and are given in Table 1. The smaller activation energy of the ferrimagnetic region suggests the hopping of electrons between the ions of different valances. The greater activation energies (>0.4 eV), obtained in the paramagnetic region, clearly indicate that the conduction is due to polar on hopping under the effect of the large thermal energy [47].

It is well known that the conduction mechanism in ferrites is predominantly due to hopping of electrons from Fe^{3+} to Fe^{2+} ions

in the octahedral sites [46,48]. The gradual decrease in the conductivity values (calculated at 1 kHz) with increasing Al-content (Table 1) can be attributed to the decrease in the total number of charge carriers. The non-multivalent nature of aluminum can reduce electron hopping through decreasing the electronic jumps between Fe^{2+} and Fe^{3+} ions [29]. It can also be noted that the activation energy is inversely proportional to the conductivity, along with the composition.

4. Conclusions

Nano-crystalline Al-substituted Mn–Zn ferrites were successfully synthesized using the citrate sol-gel method. XRD, FT-IR, TEM, VSM and AC-conductivity measurements were carried out to study structural, magnetic and electrical properties. The lattice parameters, crystallite size, saturation magnetization, coerecivity and conductivity were found to decrease by increasing the Al-content. Based on the obtained structural and magnetic data, an appropriate cation distribution of the present investigated system was suggested.

References

[1] P.P. Hankare, R.P. Patil, K.M. Garadkar, R. Sasikala, B.K. Chougule, Mater. Res. Bull. 46 (2011) 447.
[2] R. Gimenes, M.R. Baldissera, M.R.A. da Silva, C.A. da Silveira, D.A.W. Soares, L.A. Perazolli, M.R. da Silva, M.A. Zaghete, Ceram. Int. 38 (2012) 741.
[3] M. Syue, F. Wei, C. Chou, C. Fu, Thin Solid Films 519 (2011) 8303.
[4] J.S. Jang, S.J. Hong, J.S. Lee, P.H. Borse, O.S. Jung, T.E. Hong, E.D. Jeong, M.S. Won, H.G. Kim, J. Korean Phys. Soc. 54 (2009) 204.
[5] I. Sandu, L. Presmanes, P. Alphonse, P. Tailhades, Thin Solid Films 495 (2006) 130.
[6] R. Matz, D. Götsch, R. Karmazin, R. Männer, B. Siessegger, J. Electroceram. 22 (2009) 209.
[7] Y. Xuan, Q. Li, G. Yang, J. Magn. Magn. Mater. 312 (2007) 464.
[8] J. Giri, T. Sriharsha, D. Bhadur, J. Mater. Chem. 14 (2004) 875.
[9] M. George, A.M. John, S.S. Nair, P.A. Joy, M.R. Anantharaman, J. Magn. Magn. Mater. 302 (2006) 190.
[10] J. Wang, Mater. Sci. Eng., B 127 (2006) 81.
[11] P.P. Hankare, V.T. Vader, N.M. Patil, S.D. Jadhav, U.B. Sankpal, M.R. Kadam, B.K. Chougule, N.S. Gajbhiye, Mater. Chem. Phys. 113 (1) (2009) 233.

[12] P.P. Hankare, U.B. Sankpal, R.P. Patil, I.S. Mulla, P.D. Lokhande, N.S. Gajbhiye, J. Alloys Compd. 485 (2009) 798.
[13] S.Z. Zhang, G.L. Messing, J. Am. Ceram. Soc. 73 (1990) 61.
[14] J.A. Rodriguez, M. Fernandez-Garcia, Textbook of Synthesis, Properties and Applications of Oxide Nanomaterials, Wiley Interscience, A John Wiley and Sons, Inc., Publication, 2007. p. 95.
[15] H. Shokrollahi, J. Magn. Magn. Mater. 320 (2008) 463.
[16] C. Venkataraju, G. Sathishkumar, K. Sivakumar, J. Magn. Magn. Mater. 323 (2011) 1817.
[17] J. Song, L. Wang, N. Xu, Q. Zhang, J. Mater. Sci. Technol. 26 (2010) 787.
[18] T.N. Brusentsova, V.D. Kuznetsov, J. Magn. Magn. Mater. 311 (2007) 22.
[19] C.F. Zhang, X.C. Zhong, H.Y. Yu, Z.W. Liu, D.C. Zeng, Physica B 404 (2009) 2327.
[20] E. Ateia, M.A. Ahmed, A.K. El-Aziz, J. Magn. Magn. Mater. 311 (2007) 545.
[21] T.N. Brusentsova, N.A. Brusentsov, V.D. Kuznetsov, V.N. Nikiforov, J. Magn. Magn. Mater. 293 (2005) 298.
[22] M. Arora, A. Kumara, R.P. Pant, Phys. Proc. 9 (2010) 24.
[23] M.A. Ahmed, N. Okasha, M.M. El-Sayed, Ceram. Int. 33 (2007) 49.
[24] G. Chandrasekaran, S. Selvanandan, K. ManivanNane, J. Mater. Sci. 15 (2004) 15.
[25] S.A. Saafan, A.S. Seoud, R.E. El Shater, Physica B 365 (2005) 27.
[26] M.A. Gabal, R.M. El-Shishtawy, Y.M. Al Angari, J. Magn. Magn. Mater. 324 (2012) 2258.
[27] M.A. Gabal, Y.M. Al Angari, J. Magn. Magn. Mater. 322 (2010) 3159.
[28] M. Al-Haj, J. Magn. Magn. Mater. 311 (2007) 517.
[29] I. Maghsoudi, H. Shokrollahi, M.J. Hadianfard, J. Amighian, Powder Technol. 235 (2013) 110.
[30] C.C. Wu, S. Kumarakrishan, T.O. Mason, J. Solid State Chem. 37 (1981) 144.
[31] A. Bhosale, B. Chougule, Mater. Chem. Phys. 97 (2006) 273.
[32] A. Goldman, Modern Ferrite Technology, Marcel Dekker Inc., New York, 1993.
[33] H. Kavas, A. Baykal, M.S. Toprak, Y. Kseoglua, M. Sertkol, B. Aktas, J. Alloys Compd. 479 (2009) 49.
[34] C. Yao, Q. Zeng, G.F. Goya, T. Torres, J. Liu, H. Wu, M. Ge, Y. Zeng, Y. Wang, J.Z. Jiang, J. Phys. Chem. C 111 (2007) 12274.
[35] S. Bid, S.K. Pradhan, Mater. Chem. Phys. 82 (2003) 27.
[36] S. Sakurai, S. Sasaki, M. Okube, H. Ohara, T. Toyoda, Physica B 403 (2008) 3589.
[37] M.A. Gabal, S.S. Ata-Allah, J. Phys. Chem. Solids 65 (2004) 995.
[38] J. Smith, H.P.J. Wijn, Ferrites, Philips Technical Library, Eindhovan, 1959. pp. 149.
[39] M.A. Gabal, Y.M.A. Angari, Mater. Chem. Phys. 118 (2009) 153.
[40] R. Arulmurugan, G. Vaidyanathan, S. Sendhilnathan, B. Jeyadevan, J. Magn. Magn. Mater. 298 (2006) 83.
[41] R.D. Waldron, Phys. Rev. 99 (1955) 1727.
[42] V.B. Kawade, G.K. Bichile, K.M. Jadhav, Mater. Lett. 42 (2000) 33.
[43] M. Ishaque, M.U. Islam, M. Azhar Khan, I.Z. Rahman, A. Genson, S. Hampshire, Physica B 405 (2010) 1532.
[44] W.F. Vander, G.A. Sawatzky, A.H. Morrish, Phys. Rev. 167 (1968) 533.
[45] D. Ravinder, K. Suresh, Mater. Lett. 44 (2000) 253–255.
[46] M.A. Gabal, S.A. Al-Thabaiti, E.H. El-Mossalamy, M. Mokhtar, Ceram. Int. 36 (2010) 1339.
[47] D. Ravinder, B. Ravi Kumar, Mater. Lett. 57 (2003) 1738.
[48] D. Ravinder, K. Vijaya Kumar, Mater. Lett. 49 (2001) 57.